Quaternary Science Reviews
July 2021, Volume 264 Pages 106999 (17p.)
https://doi.org/10.1016/j.quascirev.2021.106999
https://archimer.ifremer.fr/doc/00700/81171/

Pacific North Equatorial Current bifurcation latitude and Kuroshio Current shifts since the Last Glacial Maximum inferred from a Sulu Sea thermocline reconstruction

Weiss Thomas L. [1, 2, *], Linsley Braddock K. [1], Gordon Arnold L. [1, 2]

[1] Lamont-Doherty Earth Observatory of Columbia University, 61 Route 9W, Palisades, NY 10964, USA
[2] Department of Earth and Environmental Science, Columbia University, 557 Schermerhorn Hall Extension, Morningside Campus, New York, NY 10027, USA

* Corresponding author : Thomas L. Weiss, email address : tweiss@ldeo.columbia.edu

Abstract :

The meridional migration of the bifurcation latitude of the Pacific North Equatorial Current (NEC) in the western boundary of the tropical Pacific modulates the strength of the Kuroshio Current. Using salinity reanalysis data, we show the NEC bifurcation latitude also acts as the dominant control on thermocline salinity of the Sulu Sea, just west of the Philippine archipelago, by regulating influx of western Pacific thermocline water via the Luzon Strait. We used oxygen isotopes (δ18O) and Mg/Ca in the thermocline-dwelling foraminifera Globorotalia tumida from Sulu Sea sediment core MD97-2141 to determine past thermocline δ18Ow and salinity variability spanning ~20–5 ka with an average sampling interval of ~50 years and infer past changes in the NEC bifurcation latitude. Our Sulu Sea thermocline reconstruction reveals high salinity from ~18.8–15.5 ka, ~12.2–11.5 ka, and from ~9.5–8.5 ka indicating the NEC bifurcation latitude was shifted north and the Kuroshio was weak at those times. Low Sulu Sea thermocline salinity from ~13.0–12.4 ka, ~11.5–10.9 ka, and from ~8.5 ka until the end of the record at ~5.6 ka indicates the NEC bifurcation latitude was shifted south and the Kuroshio Current was relatively strong. Comparison to other paleoclimate records suggests the observed northward (southward) shifts of the NEC bifurcation latitude were driven by southward (northward) shifts of the Indo-Pacific ITCZ, consistent with modern mechanisms controlling interannual NEC bifurcation variability. The NEC bifurcation latitude shifts likely modulated northward energy transport via the Kuroshio Current and the mean temperature and salinity of the Indonesian Throughflow.

Highlights

► North Equatorial Current bifurcation latitude controls Sulu Sea thermocline salinity. ► We use foraminiferal $\delta^{18}O_w$ to reconstruct Sulu Sea thermocline conditions since 20 ka. ► Reconstructions suggest bifurcation latitude shifts during Younger Dryas and HS1. ► Reconstructions show large event during early Holocene.

Keywords : Quaternary, Paleoceanography, Equatorial pacific, Stable isotopes, North equatorial current, Sulu sea, Globorotalia tumida, Kuroshio current, Thermocline reconstructions

1. Introduction

The Pacific North Equatorial Current (NEC) flows westward as the southern limb of the North Pacific subtropical gyre (Hu et al., 2015). Upon reaching the Philippine archipelago at the

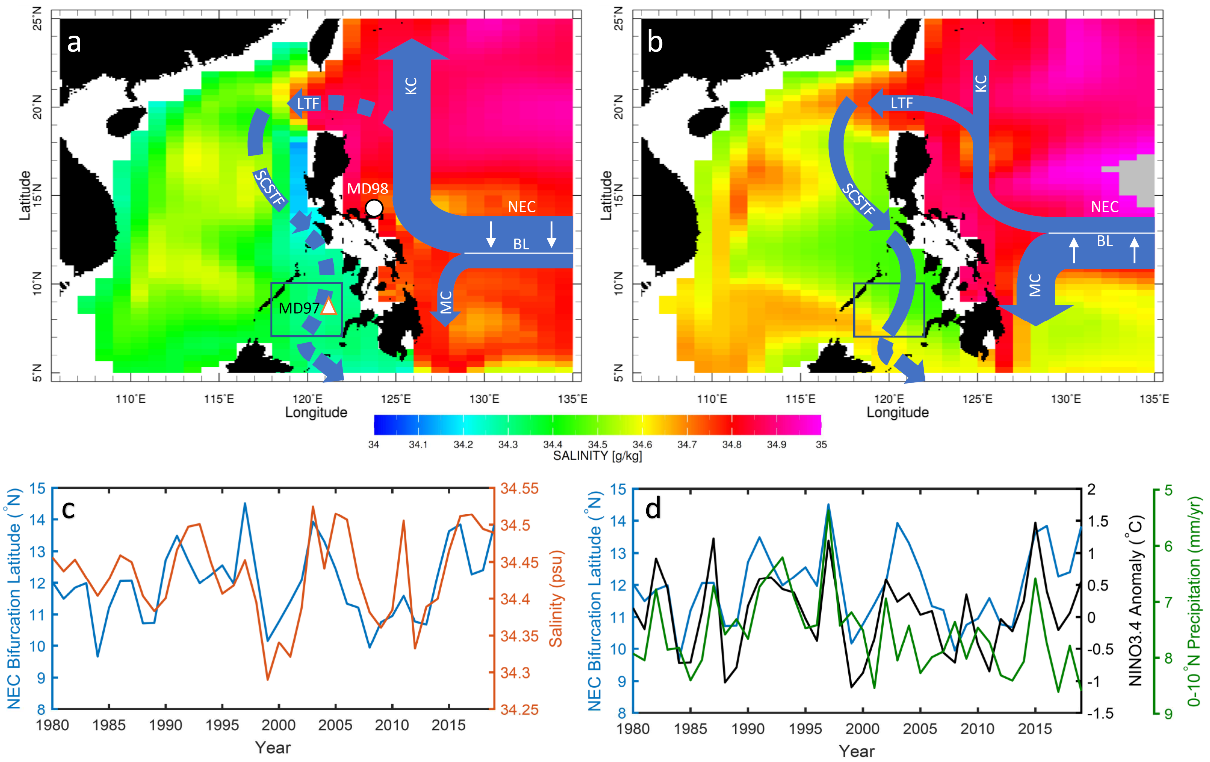

Figure 1—Geographic and temporal salinity variability associated with the NEC bifurcation latitude. a and b: GODAS (Behringer and Xue, 2004) plots of average salinity at 135 m depth for March 2000 during a strong La Niña event (a) and March 2016 during a very strong El Niño event (b). These months are representative of the salinity pattern for strong low and high salinity years. Blue arrows represent current strengths when NEC bifurcation latitude is shifted south such as during La Niña events or when the Indo-Pacific ITCZ is north (panel a) and when NEC bifurcation latitude is shifted north such as during El Niño events and when the Indo-Pacific ITCZ is shifted south (panel b). Arrow thicknesses are not quantitative and only represent relative differences in current volume and velocity between the same current in the two different panels. Over the period of 2003-2011, Luzon Strait throughflow was found to range from 2 Sv westward to 2 Sv eastward, while flow through the Sulu Sea was found to range from 8 Sv southward to 2 Sv northward (Gordon et al., 2012). As such, both currents are shown with dashed arrows in panel a to represent reversing flow. White arrows indicate the direction in which the NEC bifurcation latitude shifts. NEC: North Equatorial Current BL: NEC bifurcation latitude MC: Mindanao Current KC: Kuroshio Current LTF Luzon Strait throughflow SCSTF: SCS throughflow. The approximate locations of core MD97-2141 (white triangle with orange border) and MD98-2188 (white circle with black border) are shown in panel a. c: Average annual NEC bifurcation latitude calculated from GODAS sea surface height anomalies (Behringer and Xue, 2004) using equation two from Qui and Chen (2010) (blue). Average annual salinity from the Sulu Sea box in a and b (7°-10° N 118°-122° E) at 135 m depth (orange). d: Average annual NEC bifurcation latitude (blue) compared to average annual NINO3.4 anomaly (Rayner, 2003; Smith, 2018) (black), and average annual daily precipitation in the box 0°-10° N and 130°-160° E from GPCP Precipitation data (Adler et al., 2003) (green). Wu et al. (2019) show this index is a good indicator of the latitude of the western Pacific ITCZ and is strongly correlated to the NEC bifurcation latitude.

western boundary of the Pacific Basin, the NEC bifurcates, diverting a fraction of its waters southward to form the Mindanao Current and the remaining water northward to form the Kuroshio Current (Fig. 1). Trade wind driven changes in western Pacific wind stress curl force seasonal and interannual meridional migrations of the NEC bifurcation latitude that have a substantial impact on local and regional climate by regulating partitioning of the NEC between the Kuroshio and Mindanao currents (Hu et al., 2015) (see Table 1). For example, a more

NEC Bifurcation Latitude South	NEC Bifurcation Latitude North
Effect on the NEC: Greater Proportion is Directed North	Effect on the NEC: Greater Proportion is Directed South
How Do Currents Change: Strong Kuroshio Weak Luzon Strait Throughflow Weak South China Sea Throughflow	How Do Currents Change: Weak Kuroshio Strong Luzon Strait Throughflow Strong South China Sea Throughflow
Potential Drivers: La Niña ITCZ North PDO Negative	Potential Drivers: El Niño ITCZ South PDO Positive
Sulu Sea Thermocline Response: Relatively Fresh	Sulu Sea Thermocline Response: Relatively Salty

Table 1—Oceanographic and climatic changes associated with migrations of the NEC bifurcation latitude (Qiu and Lukas, 1996; Wu et al., 2013; Wu et al., 2019).

southerly position of the NEC bifurcation latitude diverts a larger proportion of NEC flow into the Kuroshio over the Mindanao which tends to strengthen North Pacific typhoons and enhance summer convection leading to a stronger East Asian Monsoon (Hu et al., 2015). The opposite occurs when the NEC bifurcation latitude shifts northwards. The NEC bifurcation also influences the strength and temperature of the Indonesian Throughflow (ITF), the only low latitude connection between ocean basins, by modulating the strength of flow through the Sulu Sea and thereby the development of a freshwater cap in the Makassar Strait (Gordon et al., 2012).

Given its importance in modulating the Kuroshio, ITF, and western Pacific climate, it is critical to understand the full range of NEC bifurcation latitude variability. Instrumentally, the location of the NEC bifurcation latitude can be tracked using sea surface height anomalies in the region 12°-14° N and 127°-130° E (Qiu and Chen, 2010). Sea surface height anomaly records show the NEC bifurcation latitude shifts by a couple degrees of latitude southward during boreal summer and northward during boreal winter (Gordon et al., 2012; Hu et al., 2015) (Table 1). Interannually, the NEC bifurcation latitude migrates through a larger latitudinal range between ~8°-17° N and has been shown to be controlled by a combination of El Niño-Southern Oscillation (ENSO), the Indo-Pacific Intertropical Convergence Zone (ITCZ), and the Pacific Decadal Oscillation (PDO) (Table 2) (Kim et al., 2004; Qiu and Lukas, 1996; Wu, 2013; Wu et al., 2019). The bifurcation shifts northward during El Niño events and when the ITCZ is south and southward during La Niña events and when the ITCZ is north (Qiu and Lukas, 1996; Wu et al., 2019) (Fig. 1 and Table 1).

	NINO3.4 Index	ITCZ Index	ITCZ Index (15-mth running mean)*	PDO Index
NECBL (Monthly)	0.60 ($p<0.01$)	-0.17 ($p<0.01$)		0.40 ($p<0.01$)
NECBL (Annual Avg)	0.72 ($p<0.01$)	-0.29 ($p=0.069$)	-0.48 ($p<0.01$)	0.48 ($p<0.01$)

*From Wu et al. (2019)

Table 2—NEC bifurcation latitude correlations. Correlation coefficients (r-values) from 1980-2019 between the annual average North Equatorial Current bifurcation latitude and annual averages of various climate indices. ITCZ Index is calculated as average annual daily precipitation in the box 0°-10° N and 130°-160° E (Adler et al., 2003; Wu et al., 2019).

As a result of the relative short extent of instrumental records however, it is unclear whether these relationships between the NEC bifurcation latitude and its drivers remain constant through the gamut of climate states and whether the bifurcation latitude is capable of millennial scale variability. Previously, Dang et al. (2012) generated a Mg/Ca based thermocline water temperature reconstruction using the foraminifera *Pulleniatina obliquiloculata* in IMAGES core MD987-2188 from the Pacific margin of the Philippines spanning 13-0 ka and interpreted it as a record of the NEC bifurcation latitude. As this record primarily covers the Holocene and does not extend to the Last Glacial Maximum (LGM), its utility in capturing NEC variability during climate states different from those observed in the instrumental record is limited. Several other paleo-reconstructions extending as far back as ~180 ka, use sediment provenance or foraminiferal species assemblages to monitor the strength and location of the Kuroshio Current and thus can be used to indirectly infer shifts in the NEC bifurcation latitude. However, these records were not originally intended to capture high resolution variability in the NEC bifurcation and as such, they suffer from low temporal resolution (Ujiié et al., 2016), masking of the Kuroshio signal by other controls on sediment sources (Dou et al., 2010; Chen et al., 2011; Li et al., 2015), or uncertainty in the past path of the Kuroshio Current (Dou et al., 2010; Chen et al., 2011; Li et al., 2015; Ujiié et al., 2016).

Just to the west of the Philippine archipelago the Sulu Sea, a ~4,700 m deep basin bounded entirely by islands and shallow sills with maximum sill depth of ~570 m provides a unique opportunity to generate an extended record of the NEC bifurcation latitude (Fig. 2). It has been shown that as a result of its geographic setting, a relatively limited set of mechanisms control Sulu Sea thermocline variability (Linsley and Thunell, 1990; Gordon et al., 2011) and, as we discuss below, Sulu Sea thermocline salinity variability appears to be driven by the NEC bifurcation latitude. When the NEC bifurcation latitude is north and the Kuroshio is weak, strong flow through the Luzon Strait and South China Sea (SCS) carry relatively salty open western

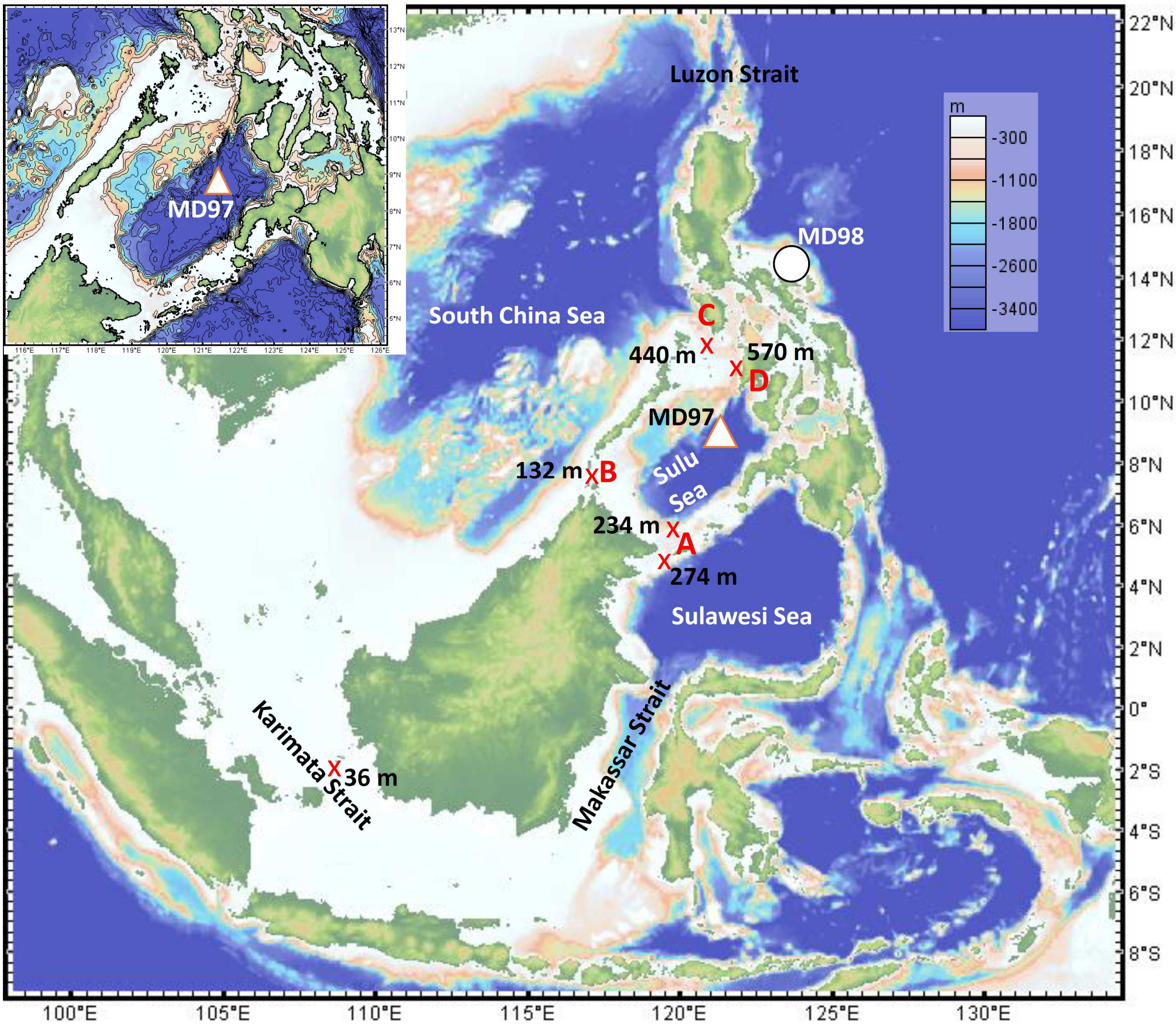

Figure 2—Location and bathymetry of the Sulu Sea in relationship to Indonesian region. X's indicate the location and depth of the shallowest points of the deepest routes water must pass to ventilate Sulu Sea deepwater and the Karimata Strait. Approximate coring locations are shown for core MD97-2141 (white triangle with orange border) and MD98-2188 (white circle with black border). A: Sibutu Passage B: Balabac Strait C: Mindoro Strait D: Panay Strait. Figure was made using the GeoMapApp: http://www.geomapapp.org (Ryan et al., 2009). Bathymetry contours (500 m intervals) and shading are from the Global Multi-Resolution Topography synthesis (GMRT) (Ryan et al., 2009) and are consistent between panels. Sulu Sea strait depths are from Gordon et al. (2011) and Karimata Strait depth is from Wang et al. (2019).

Pacific water into the SCS and Sulu Sea thermoclines (Table 1). Conversely, when the NEC bifurcation latitude is south, greatly reduced Luzon Strait and SCS throughflow increase residence times of surface and thermocline waters in the SCS and Sulu Sea and reduces the input of west Pacific water (Qu et al., 2004; Gordon et al., 2012). Zeng et al. (2016) show that strong modern Luzon Strait throughflow, also known as the Kuroshio Intrusion, results in a strong salinity maximum in the northern SCS between 120 and 150 m, while the salinity maximum is muted when Luzon Strait throughflow is weak. Luzon Strait throughflow flows through the SCS and Sulu Sea as the SCS throughflow and modern data show the strength of flow through the Luzon Strait and Sulu Sea are highly correlated (Gordon et al., 2012). As a result, variability in the SCS thermocline salinity maximum should propagate into the Sulu Sea thermocline leading to a strong correlation between Sulu Sea thermocline salinity and the NEC bifurcation latitude, the primary control on the strength of these currents.

In this study, we take advantage of this direct relationship between Sulu Sea thermocline salinity and the NEC bifurcation latitude as well as the high-resolution sediment archive in the Sulu Sea to generate a high-resolution record of NEC bifurcation latitude variability that captures a wider range of climate states than is represented by existing instrumental and paleo-records. The 36 m giant piston core IMAGES MD97-2141 (08°78'N, 121°28'E, 3,633 m depth) was retrieved during the IPHIS-IMAGES III cruise of the R/V Marion Dufresne in May 1997. We generated high-resolution $\delta^{18}O$, Mg/Ca, and trace metal records from the thermocline dwelling foraminifera *Globorotalia tumida* and *Neogloboquadrina dutertrei* (only $\delta^{18}O$) from this core spanning ~20-5 ka. In addition, we compare these records to previously published $\delta^{18}O$ and Mg/Ca records from the surface-dwelling foraminifera *Globigerinoides ruber* from the same core and samples spanning the same interval (Rosenthal et al., 2003). Modern core top studies suggest that in the Indo-Pacific, *G. tumida* calcify between 100-260 m water depth (Mohtadi et al., 2011; Hollstein et al., 2017) and *N. dutertrei* at 90-160 m (Hollstein et al., 2017). As a result, variations in thermocline salinity and temperature are recorded in the $\delta^{18}O$ of their tests and salinity variability can be decoupled from temperature fluctuations using the sensitivity of the Mg/Ca of those tests to water temperature. Because the NEC bifurcation latitude directly controls the salinity of the Sulu Sea thermocline, this sediment core record provides a unique opportunity to monitor past NEC bifurcation latitude migrations using a relatively well understood set of proxies.

1.1 Environmental Setting

Analysis of Global Ocean Data Assimilation System (GODAS) (Behringer and Xue, 2004) salinity data (Fig. A2) shows that annual average Sulu Sea thermocline salinity was significantly correlated to the annual average NEC bifurcation latitude from 1980-2019 (Fig. 1), with a maximum correlation coefficient of 0.62 (p-value<0.01) at 135 m water depth and correlation coefficients above 0.53 (p-values<0.01) between 85 m and 165 m (Table A2). GODAS SCS thermocline salinity is also significantly correlated with the NEC bifurcation latitude, but the depth of maximum correlation is slightly shallower ($r=0.65$ from 95-105 m) (Table A2). While Sulu Sea salinity at 135 m does have a moderately strong correlation to precipitation in the Sulu Sea region (7.5°-10° N, 117.5°-122.5° E) (r-value$=-0.39$, p-value$=0.01$), there is no correlation between Sulu Sea surface salinity and regional precipitation (r-value$=0.06$, p-value$=0.73$). Limitations on vertical mixing and the lack of a correlation between surface salinity and precipitation indicate the correlation between thermocline salinity and precipitation is not a result of the precipitation signal mixing from the surface to the thermocline. Furthermore, surface and thermocline salinity in the Sulu Sea are out of phase, with peak thermocline salinity occurring at the same time as the NEC bifurcation latitude reaches its northernmost latitude in November and December (Qiu and Chen., 2010) and ~10 months after peak surface salinity which occurs in March (Fig. A2). As modern local precipitation and the NEC bifurcation latitude are highly correlated to ENSO, it is likely Sulu Sea thermocline salinity is correlated to local precipitation due to their shared correlation to ENSO via different mechanisms.

The Sulu Sea is an ideal location for capturing the NEC bifurcation latitude signal in the sediment archive. Low dissolved oxygen and elevated temperatures in Sulu Sea deep water lead to reduced rates of bioturbation (mixing coefficient <0.04 cm^2/year below 3,000 m water depth) (Kuehl et al., 1993), and excellent $CaCO_3$ preservation coupled with relatively high average sedimentation rates of >15 cm/ka (Oppo et al., 2003) and have resulted in the preservation of a high-resolution sediment archive. Core MD97-2141 was originally slab sampled at 1 cm intervals and the previously published age model indicates the core contains century-scale resolution that would be unavailable in the open ocean (de Garidel-Thoron et al., 2001; Beaufort et al., 2003; Dannenmann et al., 2003; Oppo et al., 2003; Rosenthal et al., 2003). Due to its isolation and the sensitivity of Sulu Sea thermocline salinity to changes in the NEC bifurcation latitude, high sedimentation rate of core MD97-2141, and general reduced bioturbation of Sulu Sea sediments, our paleo-record of changing Sulu Sea thermocline conditions is a novel approach to understanding past NEC bifurcation latitude variability

2. Materials and Methods

2.1 Modern Indices.

The NEC bifurcation latitude ($Y_p(t)$ (°N)) was calculated using equation 2 from Qui and Chen (2010):

$$Y_p(t) = 11.9 – 0.13 \text{ x } h'(t)$$

where h'(t) is the average monthly sea surface height anomaly in cm in the box bounded by 12-14° N and 127-130° E. Monthly sea surface height anomalies were taken from the NOAA NCEP EMS CMB GODAS: Global Ocean Data Assimilation System (Behringer and Xue, 2011) and have 1° E-W resolution and 1/3° N-S resolution prior to being averaged over the box of interest. Modern precipitation data come from the GPCP version 2.3 combined precipitation data set (Adler et al., 1997) provided by the NOAA/OAR/ESRL PSD, Boulder, Colorado, USA, from their Web site at https://www.esrl.noaa.gov/psd/. Spatial resolution is 2.5x2.5° before being averaged over the area of interest. Modern correlations (r-values) and their significance (p-values) were calculated using the "corrcoef" function in Matlab.

2.2 Age Model

The age model for core MD97-2141 was originally published in de Garidel-Thoron et al. (2001) and subsequently used in Rosenthal et al. (2003). We update the age model using the original uncalibrated radiocarbon dates (Table A1) and the Marine13 calibration curve from CALIB 7.04 (Stuvier et al., 2020). The updated age model was generated using linear interpolation between the same 13 AMS radiocarbon dates used in the original age model. The default CALIB 7.04 time-dependent reservoir correction of ~400 years was applied to the calibration. Tie point calibration errors range from 51-245 years. Once interpolated to cm resolution, the updated age model ranges from ~460 years older than the original age model at ~19.7 ka to ~100 years younger than the original age model at ~14 ka. The topmost sample (0-1cm) from core MD97-2141 dates to 4.29 ka indicating a disturbance of the top of the sediment column during the coring process. Below the core top, the core was slab sampled at 1cm intervals (average temporal resolution of 48 years per sample) for the results previously published in de Garidel-Thoron et al. (2001), Rosenthal et al. (2003) and Oppo et al. (2003).

2.3 Stable Isotopes.

Eleven *G. tumida* in the 400-600 µm size fraction and 11 *N. dutertrei* in the 250-400 µm size fraction were picked from each 1-cm interval sample for stable oxygen ($\delta^{18}O$) and carbon ($\delta^{13}C$) isotope analysis. To ensure that only foraminifera of a specific morphotype, narrow size range, with no secondary calcification were analyzed, we used a Keyence VHX-5000 Digital Microscope to view and sort all foraminifera. Minimum and maximum diameters were measured on all foraminifera utilizing the maximum-area-measurement application and all were viewed under high magnification (100x-200x) to select only the most pristine foraminifera tests. Specimens that did not meet the narrow selection criteria were not geochemically analyzed. Because *G. tumida* were discolored in the top 33 cm of the core (<5.63 ka), those samples were excluded from analysis. To minimize the selective loss of fine test fragments that would bias the geochemical results, specimens were not cleaned prior to stable isotope analysis. For each sample, the scanned set of 11 foraminifera was finely crushed and homogenized, and 50-80 µg of mixed fragments were randomly selected for stable isotopic analysis.

Samples were analyzed for $\delta^{18}O$ and $\delta^{13}C$ at the Lamont-Doherty Earth Observatory (LDEO) Stable Isotope Lab using a Thermo DeltaV+ mass spectrometer with a Kiel IV autosampler device. Samples were dissolved in ~105% dewatered H_3PO_4 at 70°C, and the resulting gas was cryogenically stripped of H_2O and the purified CO_2 analyzed. Results are reported in per mil (‰) vs VPDB. The international standard NBS-19 was analyzed every ~tenth sample and had a standard deviation of 0.07‰. Approximately 10% of all samples (44 total replicates) were analyzed in replicate and were sourced from the same homogenized fragments. The mean difference between replicates was 0.11‰. Samples from 142-156 cm (10.94-11.26 ka) were picked and analyzed in duplicate in order to determine the validity of the decrease in $\delta^{18}O$ that begins at ~11.3 ka. Mean values of replicates and duplicates in the 10.94-11.26 ka interval are plotted in all figures.

2.4 Trace Metals.

For trace metal analysis, the Keyence VHX-5000 Digital Microscope was again used to select eleven clean *G. tumida* in the 400-600 μm size fraction from samples at 1 cm intervals from 34-282 cm (5.61-17.59 ka) and 2 cm intervals from 285-333 cm (17.7-19.52 ka). The 11 selected individual foraminifera tests (~500 μg) were gently cracked open and washed using the methods of Yu et al. (2005) and a combination of Barker et al. (2003) and Rosenthal et al. (1997). This method involves a reductive cleaning step using a solution of hydrazine, citric acid, and ammonium hydroxide to remove metal oxides, followed by an oxidative cleaning step using sodium hydroxide and hydrogen peroxide to remove organics. The cleaned fragments were then dissolved in trace metal clean 0.065N HNO3 (OPTIMA®). Trace metal analyses were performed at the Lamont-Doherty Earth Observatory (LDEO) Trace Metal Lab using a ThermoScientific iCAPQ Q-ICP-MS in conjunction with a HEPA-filtered enclosed autosampler. An aliquot of each sample was first analyzed to determine its Ca concentration. For final analyses, samples were then diluted to ~50 ppm Ca with 0.065N HNO_3 (OPTIMA®) to avoid matrix effects within the plasma that would result from variable Ca concentrations (Rosenthal et al., 1999).

Eight standards with a range of trace metal ratios were analyzed prior to each sample run to calibrate the sample analyses. Results were also linearly corrected for drift using quality control standards bracketing every 10 samples. Two process blanks were analyzed every instrument run in order to correct for instrument noise and contamination. Three standards with different trace metal ratios were analyzed every ~9 samples to determine precision. Average analytical precision (RSD) for the three standards was ≤0.55% for Mg/Ca. Furthermore, ~10% of samples were run in replicate and root mean squared deviation (RMSD) was 4% for Mg/Ca.

Following the methods of Schmidt et al. (2004), washing efficacy was determined by monitoring Fe/Ca and Al/Ca ratios and all samples with anomalously high values (>40 µm/mol for Al/Ca and >18 µm/mol for Fe/Ca) of either trace metal ratio were discarded. Anomalous Mg/Ca values >0.4 mmol/mol different from nearby data points were also discarded. Mg/Ca shows no correlation to Fe/Ca or Al/Ca (Fig. A1), suggesting mineral phases including these elements do not affect Mg/Ca (Schmidt et al., 2004).

2.5 Mg/Ca-based Temperature and Seawater $\delta^{18}O$ Calculations.

Estimates of past changes in water temperature were calculated from *G. tumida* Mg/Ca using the Anand et al. (2003) multi-species calibration. Although the Hollstein et al. (2017) calibration was generated using modern core-top sediments from the Philippines and Papua New Guinea coasts and is species specific, they do not report species specific error estimates, resulting in error estimates of ~+/-2° C for our G. tumida Mg/Ca data. We favor the Anand et al. (2003) calibration because it produces temperature estimates only ~0.8° C colder than the Hollstein et al. (2017) *G. tumida* specific calibration, while producing a substantially smaller error of ±0.96° C. Seawater $\delta^{18}O$ ($\delta^{18}O_w$) was calculated from foraminiferal $\delta^{18}O$ ($\delta^{18}O_f$) and Mg/Ca-based temperature using the Bemis et al. (1998) low light *Orbulina universa* calibration. We add 0.27‰ from the calibration output to move the data from the PDB scale to the SMOW scale. In combination with the colder temperatures produced by the Anand et al. (2003) temperature calibration, the Bemis et al. (1998) $\delta^{18}O_w$ calibration based on a surface-dwelling species produces values that are clearly too low as the *G. tumida* record overlaps with the *G. ruber* record. We however still use the Bemis et al. (1998) calibration over a species specific calibration as it reduces the error and produces similar relative variability to species specific calibrations (exponential term of -4.8 compared to -4.95 for the Farmer et al. (2007) *G. tumida* specific calibration which has an error ~twice as large). Standard errors for both $\delta^{18}O_w$ and temperature were calculated following the methods of Mohtadi et al. (2014) using average reproducibility for $\delta^{18}O$ and RMSD for Mg/Ca and average 0.23‰ and 0.96° C respectively. $\delta^{18}O_w$ was corrected for changes in ice volume following the methods of Gibbons et al. (2014), which assumes a change in sea level from the LGM to the Holocene (ΔSL) of -130 m ±7.5 m and a change in global $\delta^{18}O_w$ ($\Delta\delta^{18}O_w$) of 1‰ ±0.1‰. The correction is then scaled through time using coral-based sea level records and assuming a constant $\Delta\delta^{18}O_w/\Delta SL$ through time. Error for the ice volume correction was also calculated following the methods of Gibbons et al. (2014). Propagated error for *G. tumida* ice volume corrected $\delta^{18}O_w$ ($\delta^{18}O_{w\text{-}IVC}$) averages 0.33‰. The $\delta^{18}O_{w\text{-}IVC}$ gradient was calculated by subtracting *G. ruber* $\delta^{18}O_{w\text{-}IVC}$ interpolated to a 50-year time step from *G. tumida* $\delta^{18}O_{w\text{-}IVC}$ calculated from low-pass filtered Mg/Ca. One per mil was added to *G. tumida* $\delta^{18}O_{w\text{-}IVC}$ so the two records don't overlap.

2.6 Low-Pass Filtering and Differences in Means

In order to isolate and interpret low frequency variability that is otherwise obscured by high frequency variability and noise, *G. tumida* $\delta^{18}O_{w\text{-}IVC}$ was low-pass filtered and *G. tumida* $\delta^{18}O_{w\text{-}IVC}$ was calculated from low-pass filtered Mg/Ca. Prior to low-pass filtering, *G. tumida*

$\delta^{18}O_{w-IVC}$ and Mg/Ca were interpolated using a spline to an even 50-year time step, slightly larger than the average sampling interval for the core during the studied interval of ~48 years per sample. Frequencies greater than 1/1,000 cycle per year were then removed using the "lowpass" Matlab filter. *G. tumida* $\delta^{18}O$ and the Gibbons et al. (2014) sea level correction were subsequently interpolated following the same methods in order to calculate *G. tumida* $\delta^{18}O_{w-IVC}$ from the filtered Mg/Ca and unfiltered $\delta^{18}O$.

Statistical significance was determined by selecting age cutoffs for the intervals that provide the greatest contrast between those that were compared. A z-score for the difference of mean *G. tumida* $\delta^{18}O_{w-IVC}$ between two intervals of interest was calculated using:

$$z = \frac{\mu_1 - \mu_2}{\sqrt{\left(\frac{e_1^2}{n_1} + \frac{e_2^2}{n_2}\right)}}$$

where μ is the mean *G. tumida* $\delta^{18}O_{w-IVC}$ for the interval of interest, e is the mean error, and n is the number of data points in the interval. For $\delta^{18}O_{w-IVC}$ calculated from low-pass filtered interpolated Mg/Ca and unfiltered interpolated $\delta^{18}O$, e and n were determined using the unfiltered $\delta^{18}O_{w-IVC}$ data from the same intervals of interest. P-values were then calculated using a one-tailed significance test. Plotted errors for these intervals were calculated as $\frac{e}{\sqrt{n}}$.

3. Results

3.1 *G. tumida* Depth Habitat

Our new $\delta^{18}O$ and Mg/Ca based temperature results from analysis of thermocline dwelling *G. tumida* in core MD972141 are compared to the similar data from the surface-dwelling foraminifera *G. ruber* extracted from the same samples (from Rosenthal et al., 2003) in Figures 3 and S4. In order to utilize our Sulu Sea *G. tumida* $\delta^{18}O_w$ results as a record of past

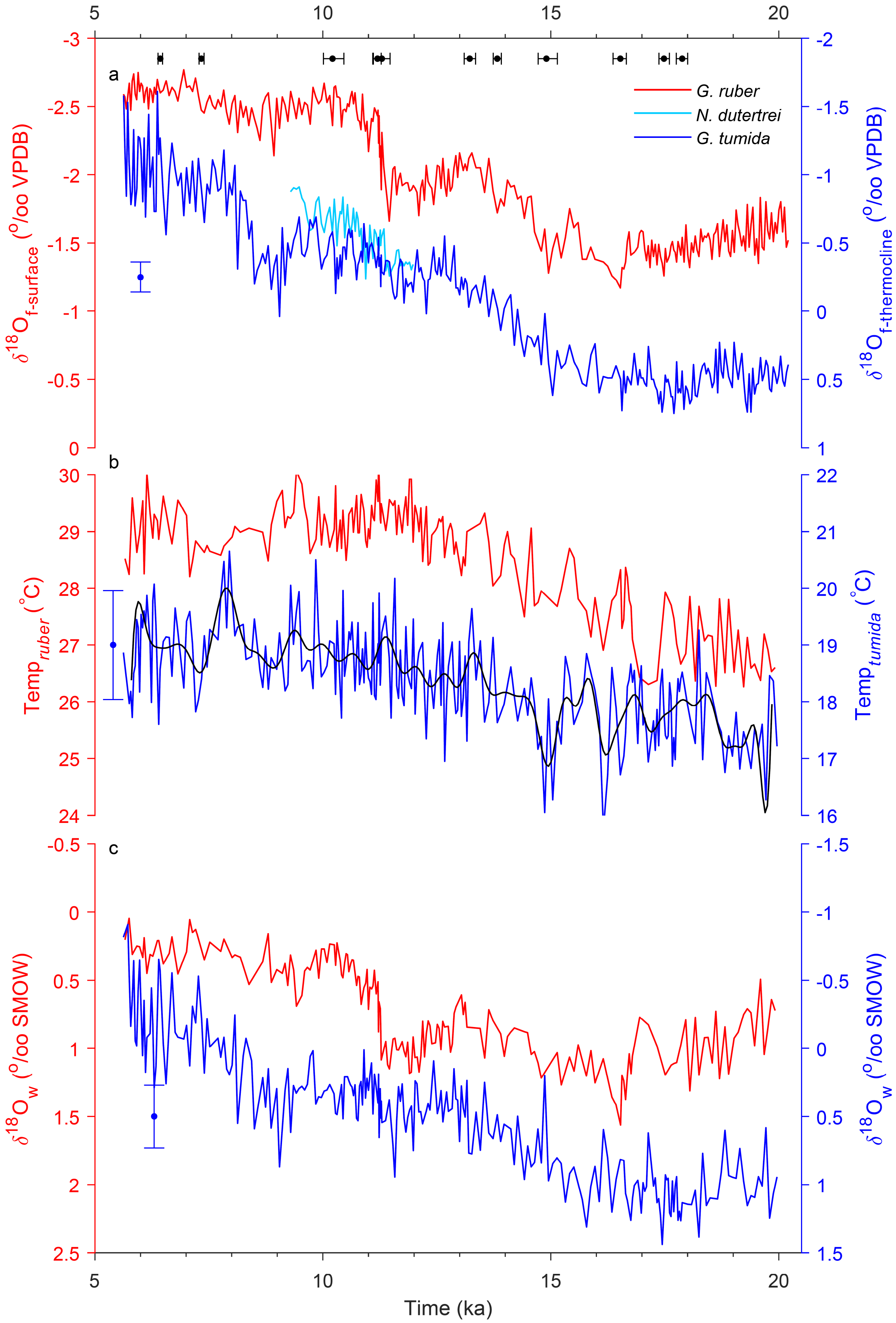
a
b
c
G. ruber
N. dutertrei
G. tumida
$\delta^{18}O_{f\text{-}surface}$ (‰ VPDB)
$\delta^{18}O_{f\text{-}thermocline}$ (‰ VPDB)
$Temp_{ruber}$ (°C)
$Temp_{tumida}$ (°C)
$\delta^{18}O_w$ (‰ SMOW)
Time (ka)

314

Figure 3—Sulu Sea foraminiferal $\delta^{18}O$, Mg/Ca based temperature, and $\delta^{18}O_w$. **a:** *G. ruber* (red), *G. tumida* (dark blue), and *N. dutertrei* (light blue) $\delta^{18}O_f$. Black dots represent age model radiocarbon tie points with 1σ error **b:** *G. ruber* and *G. tumida* Mg/Ca-based temperature and 1,00 year low-pass filtered *G. tumida* temperature (black) **c:** *G. ruber* and *G. tumida*-based $\delta^{18}O_w$. All *G. ruber* data was initially published in Rosenthal et al. (2003). Error bars for all *G. tumida* records are based on average replicate reproducibility and represent maximum error as errors vary by datum.

NEC bifurcation latitude variability, it is necessary to show that the depth habitat of *G. tumida* in the Sulu Sea can be constrained to the depth where the NEC bifurcation latitude has the greatest influence on salinity. We estimate depth habitats for Sulu Sea *G. tumida* by comparing average Mg/Ca and $\delta^{18}O$ from the youngest ~1.4 ka of our *G. tumida* records (7.01-5.63 ka) to six modern temperature and salinity profiles from the Sulu Sea (Gordon and Villanoy, 2011). When compared to modern temperature profiles, average Mg/Ca based temperature from the youngest ~1.4 ka of our record of 18.91±1.12° C suggests *G. tumida* in the Sulu Sea calcify at a mean depth of ~135 m (120-148 m 1σ), in the center of the depth range that shows the strongest correlation to the NEC bifurcation latitude (Fig. 4). To estimate a depth habitat from $\delta^{18}O$, we assume *G. ruber* live at the shallowest depth for each profile (0 -2 m) and assign average *G. ruber* $\delta^{18}O$ from 7.01-5.63 ka as the expected foraminiferal $\delta^{18}O$ for that depth. Assuming slopes of -0.22 ‰/°C and the surface and subsurface $\delta^{18}O$ vs salinity slopes of 0.33 ‰/salinity unit and 0.37 ‰/salinity unit (from Hollstein et al. (2017) who used modern instrumental salinity and $\delta^{18}O$ data from the Philippines and New Guinea margins), we calculate expected foraminiferal $\delta^{18}O$ profiles for both the surface and subsurface salinity slopes. Both the surface and subsurface $\delta^{18}O$ vs salinity relationships indicate *G. tumida* calcify at ~107 m (102-113 m 1σ) in the Sulu Sea. Similar $\delta^{18}O$ values of Sulu Sea *G. tumida* and shallow dwelling *N. dutertrei* (reported depth range of 90-160 m (Figure 3a) (Hollstein et al., 2017)) further support our estimated depth range. While our estimated calcification depths for Sulu Sea *G. tumida* based on Mg/Ca and $\delta^{18}O$ do not overlap, both clearly fall into the depth range where Sulu Sea salinity is strongly correlated to the NEC bifurcation latitude and we therefore conclude that Sulu Sea *G. tumida* are ideal for capturing millennial scale NEC bifurcation latitude variability.

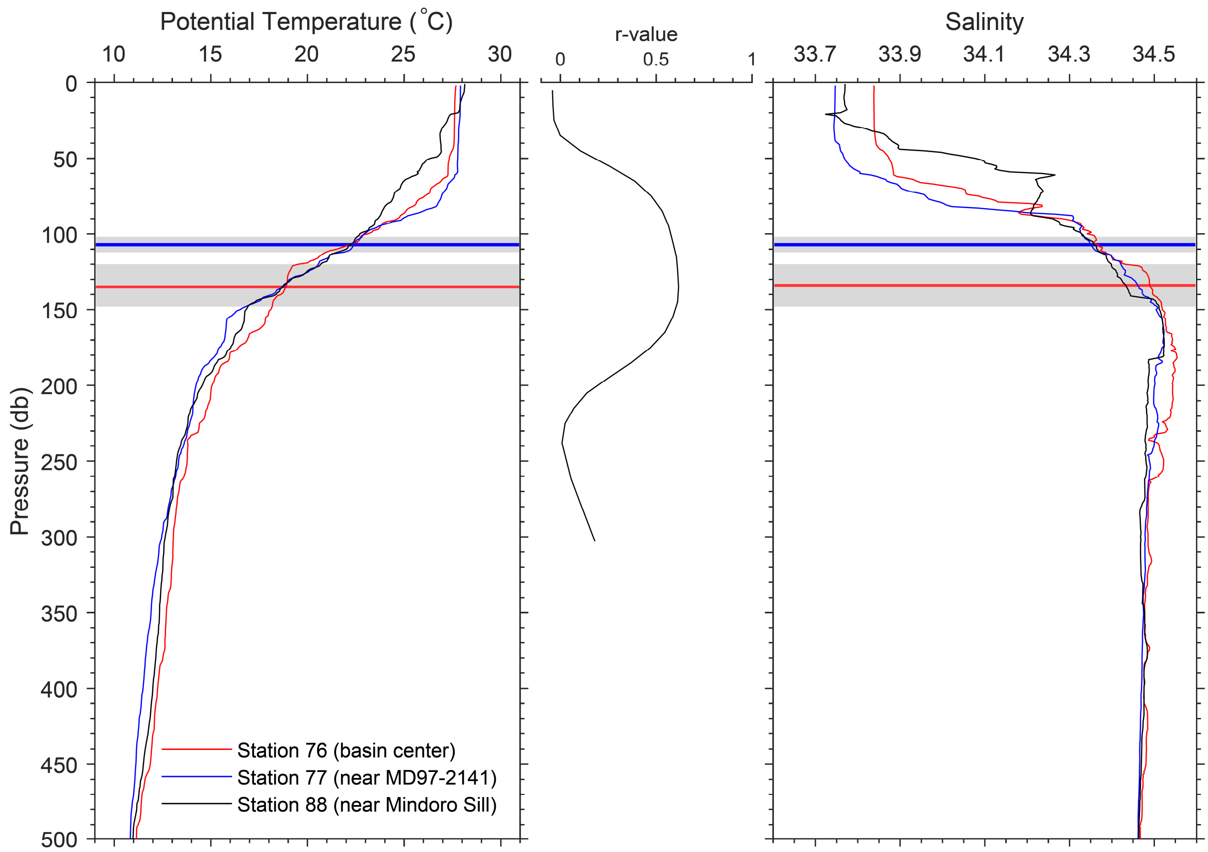

Figure 4—Potential temperature and salinity profiles from the Sulu Sea. Data and station numbers are from Gordon and Villanoy (2011). Stations 76 and 77 were sampled on 1/18/08. Station 88 was sampled 1/20/08. Approximate depth habitat of *G. tumida* based on our Mg/Ca based temperature record is highlighted in gray with the mean in red and based on $\delta^{18}O$ with the mean in blue. The r-value plot shows the correlation between annual average Sulu Sea salinity at each depth and the annual average NEC bifurcation latitude.

3.1 MD97-2141 Paleo-Data

Similar to *G. ruber* $\delta^{18}O$, *G. tumida* $\delta^{18}O$ shows a clear glacial-interglacial cycle with smaller magnitude millennial scale variability (Fig. 3a). *G. tumida* $\delta^{18}O$ shows a larger glacial interglacial amplitude of ~1.5‰ than *G. ruber* which has a glacial interglacial amplitude of ~1‰ (Rosenthal et al., 2003) (Fig. 3a). We interpret *G. tumida* Mg/Ca (Fig. A4)) to primarily be a record of water temperature and to be minimally impacted by salinity and dissolution (see appendix A). In contrast to $\delta^{18}O$, the glacial-interglacial thermocline temperature signal derived from *G. tumida* of <2°C is smaller than the ~2.3° C amplitude derived from *G. ruber* (Rosenthal et al., 2003) (Fig. 3b). Minimal millennial scale variability in our *G. tumida* Mg/Ca (Fig. 3b) based temperature record, (all variability is smaller than the propagated error), indicates Sulu Sea thermocline $\delta^{18}O$ variability was primarily driven by changes in $\delta^{18}O_w$ (Fig. 3a). Though *G. tumida* based $\delta^{18}O_w$ takes incorporates the Mg/Ca based temperature record, it still shows similar variability to *G. tumida* $\delta^{18}O_f$ (Fig. 3c).

We apply an ice volume correction (IVC) to account for changes in global seawater $\delta^{18}O_w$ due to deglacial ice melt (Fig. 5a). Because $\delta^{18}O_w$ is linearly related to salinity (Craig and Gordon, 1965; Hollstein et al., 2017), we attribute millennial scale shifts in *G. tumida* derived $\delta^{18}O_{w\text{-}IVC}$ to changes in local salinity. Low-pass filtered *G. tumida* $\delta^{18}O_{w\text{-}IVC}$ is shown in Figure 5 a and b and *G. tumida* $\delta^{18}O_{w\text{-}IVC}$ calculated from low-pass filtered Mg/Ca and unfiltered $\delta^{18}O$ is shown in Figure 5b. Both records display a minimum from the beginning of the records at ~19.6 ka until they rapidly increase by ~0.4‰ at ~18.8 ka. $\delta^{18}O_{w\text{-}IVC}$ remains elevated until 15.5 ka when it abruptly increases by ~0.3‰, resulting in a broad maximum that we interpret as a thermocline salinity maximum in the Sulu Sea. Following the abrupt decrease ~15.5 ka, Sulu Sea low-pass filtered *G. tumida* $\delta^{18}O_{w\text{-}IVC}$ and *G. tumida* $\delta^{18}O_{w\text{-}IVC}$ calculated from low-pass filtered Mg/Ca decrease to a minimum from ~13-12.4 ka. Consistently elevated $\delta^{18}O_{w\text{-}IVC}$ values ~0.3‰ greater those during the previous interval occur from 12.2-11.3 ka. This is accompanied by *G. ruber* $\delta^{18}O_{w\text{-}IVC}$ that is ~0.5‰ higher than the previous interval (Fig. 5b and 5c). At ~11.5 ka, *G. tumida* $\delta^{18}O_{w\text{-}IVC}$ decreases by ~0.4‰, accompanied by a decrease in *G. ruber* $\delta^{18}O_{w\text{-}IVC}$ of about

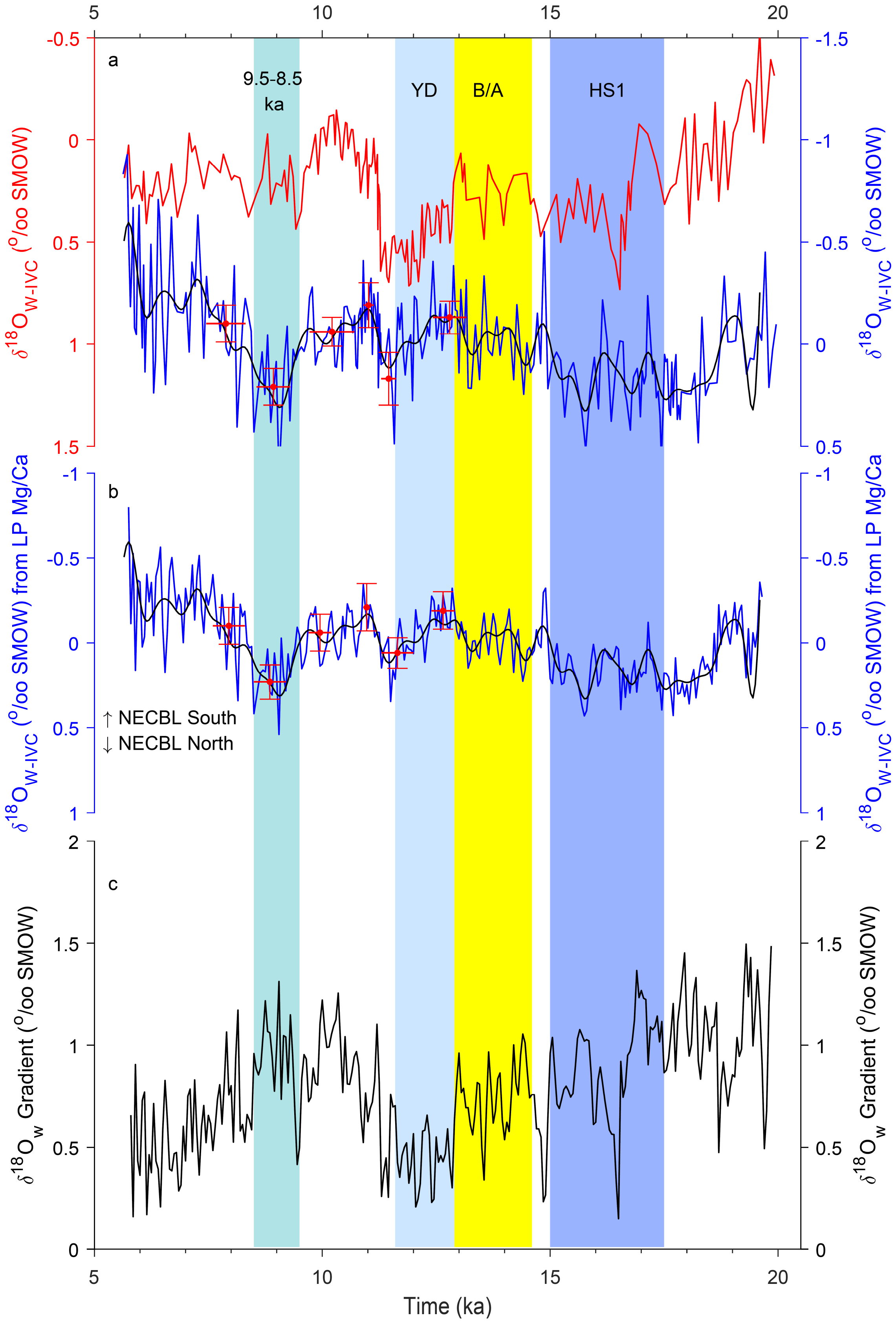

a
b
c
9.5-8.5 ka
YD
B/A
HS1
$\delta^{18}O_{W\text{-}IVC}$ (°/oo SMOW)
$\delta^{18}O_{W\text{-}IVC}$ (°/oo SMOW) from LP Mg/Ca
↑ NECBL South
↓ NECBL North
$\delta^{18}O_w$ Gradient (°/oo SMOW)
Time (ka)

367

Figure 5— Ice Volume corrected foraminiferal $\delta^{18}O_w$.**a:** *G. tumida* (blue) and *G. ruber* (red) $\delta^{18}O_{w\text{-}IVC}$ and 1,000 year low-pass filtered *G. tumida* $\delta^{18}O_{w\text{-}IVC}$ (black). **b:** *G. tumida* $\delta^{18}O_{w\text{-}IVC}$ calculated using 1,000 year low-pass filtered Mg/Ca and unfiltered $\delta^{18}O$ (blue) and 1,000 year low-pass filtered *G. tumida* $\delta^{18}O_{w\text{-}IVC}$ (same as in a) (black). Red horizontal bars in a and b represent the time step for which average *G. tumida* $\delta^{18}O_{w\text{-}IVC}$ was calculated for the respective data sets. **c.** Sulu Sea surface ocean to thermocline $\delta^{18}O_w$ gradient calculated as the *G. tumida* $\delta^{18}O_{w\text{-}IVC}$ from low-pass filtered Mg/Ca and *G. ruber* $\delta^{18}O_{w\text{-}IVC}$ difference. Vertical colored bars represent the timing of significant climatic events discussed in the text. HS1: Heinrich Stadial 1 B/A: Bølling-Allerød YD: Younger Dryas Chronozone. Note that the timing indicated for Heinrich Stadial 1, the Younger Dryas, and the Bølling-Allerød reflects the generally accepted age of these events, not necessarily in timing reflected in the Sulu Sea. For example, the Bølling-Allerød and Younger Dryas Chronozone events in our record are delayed relative to the corresponding chronozones

0.5‰. After 10.9 ka, Sulu Sea thermocline $\delta^{18}O_{w\text{-}IVC}$ increased gradually until abruptly increasing by ~ 0.3‰ at ~9.5 ka and remaining elevated until ~8.5 ka. This increase in Sulu Sea thermocline $\delta^{18}O_{w\text{-}ICV}$ indicates an increase in thermocline salinity that was substantially larger than the muted response in the mixed layer which shows a ~0.1‰ increase in *G. ruber* $\delta^{18}O_{w\text{-}IVC}$ ~9.1-8.9 ka (Fig. 3c). Following this period of relatively elevated Sulu Sea thermocline salinity, *G. tumida* $\delta^{18}O_{w\text{-}IVC}$ decreases by 0.6‰ beginning at ~8.5 ka, indicating a freshening in the Sulu Sea thermocline in the mid-Holocene that continued to the youngest interval of our reconstruction at 5.6 ka.

4. Discussion

4.1 Evidence of NEC Bifurcation Latitude Variability Since the LGM

Substantial millennial scale variability in our Sulu Sea *G. tumida* $\delta^{18}O_{w\text{-}IVC}$ record suggests that the Pacific NEC bifurcation latitude did indeed undergo millennial scale migrations. Elevated low-pass *G. tumida* $\delta^{18}O_{w\text{-}IVC}$ and *G. tumida* $\delta^{18}O_{w\text{-}IVC}$ calculated from low-pass Mg/Ca indicate that Sulu Sea thermocline salinity experienced a maximum from ~18.8-15.5 ka (Fig. 5c). This maximum is not mirrored in *G. ruber* $\delta^{18}O_{w\text{-}IVC}$ which instead steadily increases during this interval from a minimum at ~20 ka (Fig. 5a), supporting our conclusion that precipitation signals are unable to mix to the thermocline and therefore, precipitation variability was not driving the increase in *G. tumida* $\delta^{18}O_{w\text{-}IVC}$ during the ~18.8-15.5 ka interval. An argument could be made that lower sea level during this interval affected Sulu Sea thermocline salinity as it nearly closed the Balbac Strait which has a maximum depth of ~131 m (Fig. 2) (Sathiamurthy and Voris, 2006; Gordon et al., 2012). However, the deepest modern passage through the Mindoro Strait is ~440 m, meaning even with a maximum potential LGM sea level change amplitude of ~118-135 m (Clark and Mix, 2002; Yokoyama et al., 2018), the passage was still deeper than the depth habitat of *G. tumida*. The same can be said about the far deeper and wider Luzon Strait. Rosenthal et al. (2003) do attribute relatively fresh conditions in the Sulu Sea surface during the LGM to low sea level directing a larger proportion of relatively fresh SCS outflow into the Sulu Sea by closing the Karimata Strait which is currently ~36 m deep. As the modern depth habitat of *G. tumida* is already substantially lower than the depth of the Karimata Strait, it is unlikely closing the strait would have any influence on *G. tumida* $\delta^{18}O_{w\text{-}IVC}$. Having ruled out precipitation and sea level as drivers, we attribute the increase in Sulu Sea thermocline salinity from ~18.8-15.5 ka to a prolonged northward shift of the NEC bifurcation latitude weakening the Kuroshio and strengthening Luzon Strait and SCS throughflow, confirming that the NEC bifurcation latitude can experience prolonged millennial scale shifts during colder climate states. Foraminiferal species assemblage and Mg/Ca data from two sediment cores south of Japan (Ujiié et al., 2016) and sediment provenance studies from the Okinawa Trough (Chen et al., 2011; Li et al., 2015) are consistent with our interpretation, showing evidence of a weaker Kuroshio current for the duration of the LGM.

Elevated average unfiltered *G. tumida* $\delta^{18}O_{w\text{-}IVC}$ and $\delta^{18}O_{w\text{-}IVC}$ calculated from low-pass Mg/Ca during ~12.2-11.5 ka are significantly different from the prior minimum from ~13.0-12.4

ka and the following minimum after ~11.5 ka at $p \leq 0.051$ (Fig 5b) (Table A3), indicating that Sulu Sea thermocline salinity was high during that period. Given that the Luzon Strait and all the passages between the SCS and Sulu Sea would have been open and that the Karimata Strait was not open for the duration of these intervals (Sathiamurthy and Voris, 2006; Gordon et al., 2012), we do not think sea level played any role in modulating Sulu Sea thermocline. Rosenthal et al. (2003) attribute the concurrent much larger peak in Sulu Sea surface salinity from ~13.8-12 ka to a reduction in precipitation during the Younger Dryas Chronozone. They attribute the minima in salinity before and after the Younger Dryas Chronozone to elevated precipitation during the Bølling-Allerød and early Holocene. These inferred changes in precipitation are all evident in Chinese speleothem monsoon paleoclimate records. Any precipitation/runoff related salinity anomalies would easily have been advected at the surface from the SCS to the Sulu Sea with a closed Karimata Strait (Cheng et al., 2016) (Fig. 6b). As stated earlier however, limitations of vertical mixing and modern instrumental data suggest the precipitation signal observed in the Sulu Sea surface could not have mixed to the thermocline to be captured by our *G. tumida* $\delta^{18}O_{w-IVC}$ records. Instead, we attribute the maximum in thermocline salinity from ~12.2-11.5 ka to a prolonged northward shift of the NEC bifurcation latitude and the minima in salinity from ~13.0-12.4 ka and after ~11.5 ka to southward migrations of the NEC bifurcation latitude. These shifts in the NEC bifurcation latitude would be accompanied by a weakened Kuroshio Current from ~12.2-11.5 ka and a strengthened current from ~13.0-12.4 ka and after ~11.5 ka. Based on modern precipitation driven Sulu Sea surface salinity variability being larger than modern NEC bifurcation latitude driven thermocline variability, a reduction in the surface to thermocline

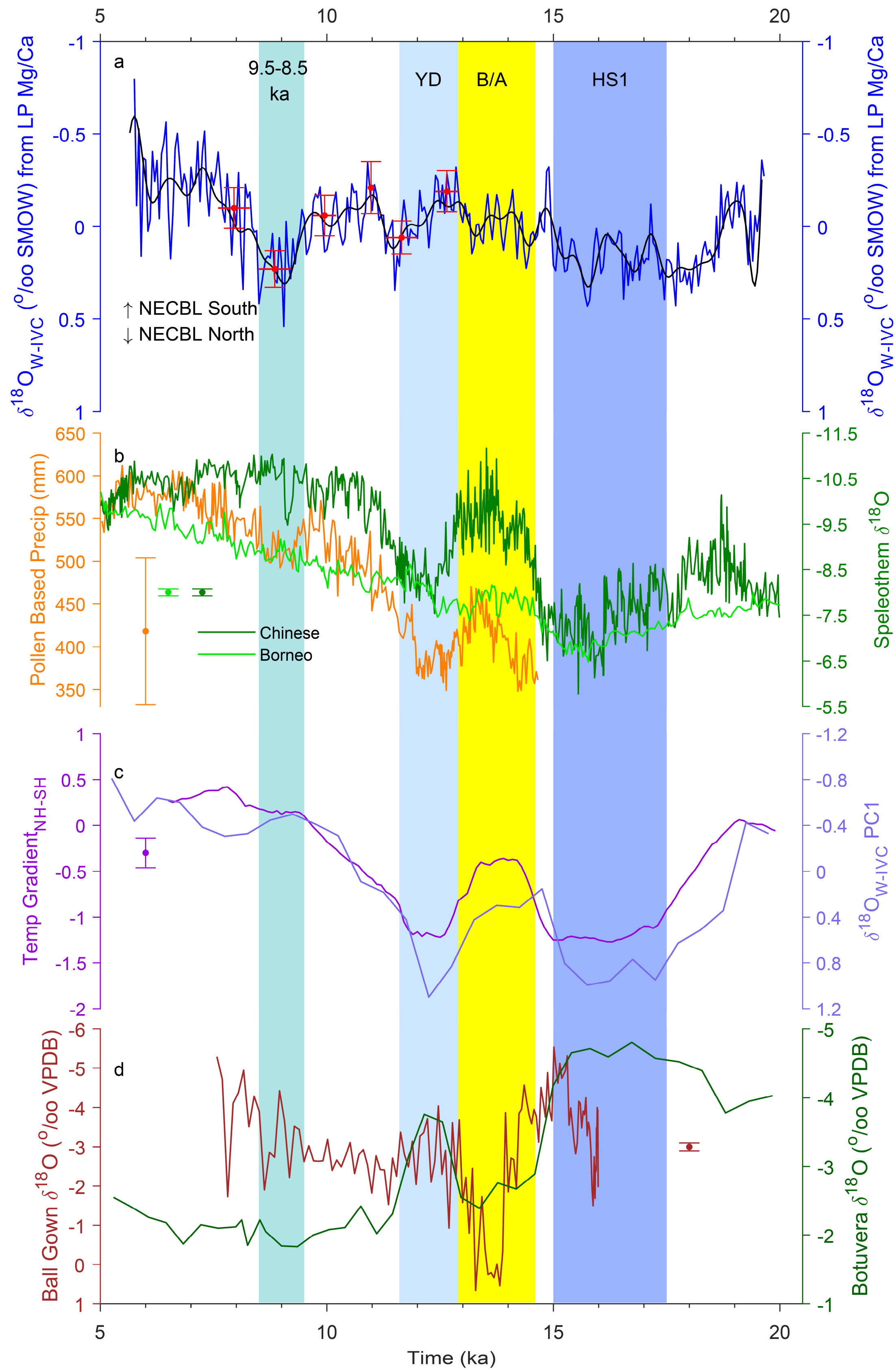
a
9.5-8.5 ka
YD
B/A
HS1
↑ NECBL South
↓ NECBL North
δ18OW-IVC (o/oo SMOW) from LP Mg/Ca
b
Pollen Based Precip (mm)
Chinese
Borneo
Speleothem δ18O
c
Temp GradientNH-SH
δ18OW-IVC PC1
d
Ball Gown δ18O (o/oo VPDB)
Botuvera δ18O (o/oo VPDB)
Time (ka)

430

Figure 6—Comparison of Sulu Sea *G. tumida* $\delta^{18}O_{w\text{-}IVC}$ to other regional climate records. **a:** *G. tumida* $\delta^{18}O_{w\text{-}IVC}$ calculated using 1,000 year low-pass filtered Mg/Ca and unfiltered $\delta^{18}O$ (blue) and 1,000 year low-pass filtered *G. tumida* $\delta^{18}O_{w\text{-}IVC}$ (black). Red horizontal bars indicate the interval over which average *G. tumida* $\delta^{18}O_{w\text{-}IVC}$ was calculated **b:** composite Chinese speleothem $\delta^{18}O$ record (Cheng et al., 2016) (dark green), Borneo speleothem $\delta^{18}O$ (Partin et al., 2007) (light green) and pollen-based precipitation estimates from a northern Chinese lake (Chen et al., 2015) (orange) **c:** interhemispheric temperature gradient (Shakun et al., 2012) (dark purple) and a compilation of surface $\delta^{18}O_{w\text{-}IVC}$ records from the equatorial Pacific (Gibbons et al., 2014) (light purple) **d:** northern Australia speleothem $\delta^{18}O$ from Ball Gown Cave (Denniston et al., 2013) (brown) and Brazilian speleothem $\delta^{18}O$ from Botuvera Cave (Wang et al., 2007) (green).

$\delta^{18}O_{w\text{-}IVC}$ gradient when salinity was high from ~12.2-11.5 ka and increases in the gradient when conditions were relatively fresh from ~13.0-12.4 ka and after ~11.5 ka support out interpretation that precipitation controlled surface salinity and the NEC controlled thermocline variability (Fig. 5c).

In agreement with our Sulu Sea thermocline record, Philippine margin thermocline temperature suggests the NEC bifurcation latitude was shifted north from ~12.2-11.5 ka (Dang et al., 2012) (Fig. 7) and Okinawa Trough sediment provenance (Cheng et al., 2016) indicates a weakened Kuroshio current during that interval. Low temporal resolution likely precludes the Ujiié et al. (2016) Kuroshio strength reconstruction from capturing this event while the event may be obscured by other controls on sediment provenance in other records (Dou et al., 2010; Chen et al., 2011; Li et al., 2015).

The largest excursions in our reconstruction of Sulu Sea thermocline $\delta^{18}O_w$ are the increasing $\delta^{18}O$ and $\delta^{18}O_w$ conditions from ~9.5-8.5 ka indicating relatively salty conditions in the Sulu Sea thermocline followed by a prolonged decrease in $\delta^{18}O_w$ and freshening from ~8.5 ka to the end of the record (Fig. 5c). The difference in mean value for the 9.5-8.5 ka interval and the intervals before and after in the unfiltered $\delta^{18}O_{w\text{-}IVC}$ record (Fig. 5a) and $\delta^{18}O_{w\text{-}IVC}$ calculated from low-pass filtered Mg/Ca (Fig. 5b) represented by horizontal red bars are statistically

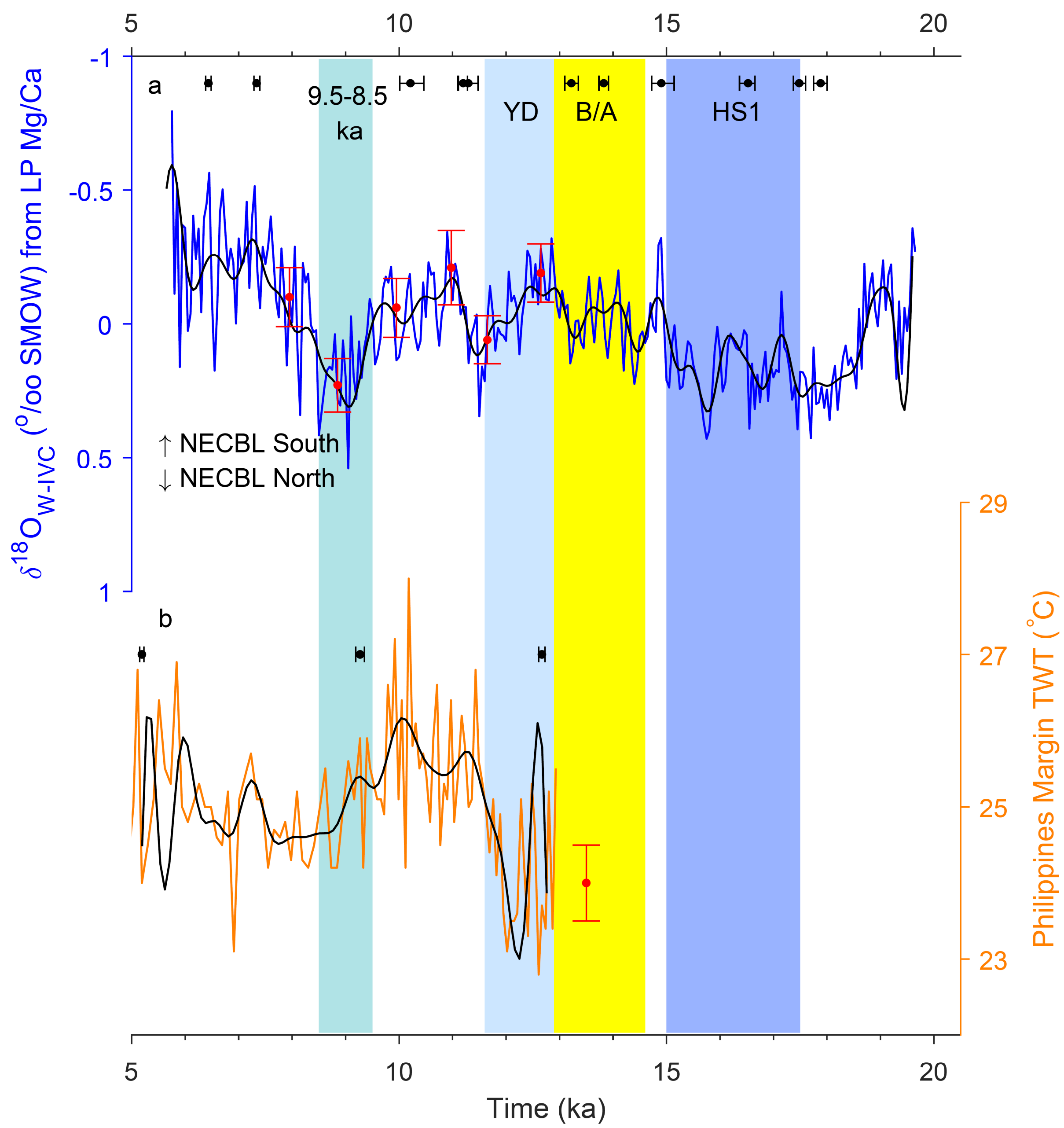

Figure 7—Comparison of Sulu Sea *G. tumida* $\delta^{18}O_{w\text{-}IVC}$ to Philippine margin conditions. **a:** *G. tumida* $\delta^{18}O_{w\text{-}IVC}$ calculated using 1,000 year low-pass filtered Mg/Ca and unfiltered $\delta^{18}O$ (blue) and 1,000 year low-pass filtered *G. tumida* $\delta^{18}O_{w\text{-}IVC}$ (black) **b)** Philippines margin thermocline water temperature from Dang et al. (2012). The record is plotted with a 1,000 year low-pass filter in black. Tie points for the age model used in Dang et al. (2012) and generated in Lin et al. (2006) are shown in black with analytical error.

different at a p-value of ≤0.05 (Table A3). Linsley et al. (2010) argued that at ~9.5 ka, rising sea level open the Karimata Strait, which then began to syphon relatively freshwater through the strait and away from the Sulu Sea, freshening the Sulu Sea surface. We agree with this interpretation and attribute steadily increasing Sulu Sea surface salinity beginning at ~9.7 ka to the opening of the Karimata Strait, but as previously stated, it is unclear how the ~36 m deep Karimata Strait could affect *G. tumida* with its substantially deeper depth habitat. As it is clear precipitation doesn't mix to the thermocline and furthermore and proximal speleothem-based precipitation records from China and Borneo don't show minima from ~9.5-8.5 ka or increase after ~9.5 ka, we attribute the salinity maximum in the Sulu Sea thermocline from ~9.5-8.5 ka to a northward shift in the NEC bifurcation latitude and a weakened Kuroshio Current and the proceeding freshening in the thermocline to a southward shift in the NEC bifurcation latitude and a weakening Kuroshio. Because only the thermocline responded to these events, opposite to the salinity variability that occurred from ~13.0-11.5 ka, the increase in thermocline salinity from ~9.5-8.5 ka increased the thermocline gradient and the decrease reduced the gradient.

To our knowledge, similar increases in thermocline salinity during the ~9.5-8.5 ka interval have not been identified in any other Indo-Pacific thermocline paleo-salinity records (Xu et al., 2008; Holbourn et al., 2011; Sagawa et al., 2012; Xu, 2014). The limited regional extent of this salinity event would be consistent with our interpretation that strengthened SCS throughflow due to a northward shift in the NEC bifurcation latitude decreased Sulu Sea thermocline salinity. Philippine margin thermocline water cooled at ~9.8 ka (Fig. 7), indicating a northward shift in NEC bifurcation latitude ~300 years prior to our record (Dang et al., 2012), a small age offset considering the age model for Philippine margin core MD98-2188 has only three tie points between 13-3 ka (Fig. 7b) (Dang et al., 2012), while our age model for core MD97-2141 has no tie points between 10-7.5 ka (Fig.7a). Warming is observed in the Philippine margin core, suggesting a southward shift of the NEC bifurcation latitude from ~8-5 ka, again a small age offset from our record considering age model uncertainties.

4.2 Controls on the NEC Bifurcation Latitude Through Time

4.2.1 The Indo-Pacific ITCZ

Having shown that several millennial scale shifts in the NEC bifurcation latitude have occurred since the LGM, we seek to determine whether those shifts can be attributed to similar drivers as shifts in the NEC bifurcation identified in instrumental records and if so, whether there was a dominant driver. The timing of the inferred northerly position of the NEC bifurcation during at ~18.5-15.5 ka corresponds approximately to that of Heinrich Stadial 1 (HS1) (17.5-15 ka (McManus et al., 2004)). While HS1 is theorized as a cooling of the North Atlantic in response to a weakening of the Atlantic Meridional Overturning Circulation (AMOC) (McManus et al., 2004), several records suggest that in response to Northern Hemisphere cooling, the Indo-Pacific ITCZ shifted in concert with the global southerly shift of the ITCZ. Sediment core temperature and SSS compilations show that the Northern Hemisphere cooled on average relative to the Southern Hemisphere (Shakun et al., 2012) and suggest the ITCZ shifted southward as a result (Gibbons et al., 2014) (Fig. 6c). In agreement, speleothems from China contain evidence of reduced precipitation during HS1 (Cheng et al., 2016), while speleothems from southern hemisphere sites in Australia and Brazil show increased precipitation (Wang et al., 2007; Dennison et al., 2013) (Fig. 6b and d). The prolonged southward shift of the ITCZ during HS1 is reminiscent of the modern southward shifts of the ITCZ that have been shown by instrumental records to drive northward migrations of the NEC bifurcation latitude through their modulations of the Indo-Pacific wind field (Wu et al., 2019). We therefore hypothesize that it was this shift in the Indo-Pacific ITCZ that drove the northward migration of the NEC bifurcation latitude at ~18.5-15.5 ka.

Similar Indo-Pacific and global ITCZ variability is observed during the ~13.0-11.5 ka interval. During the Younger Dryas (12.9-11.6 ka), a weakened AMOC is hypothesized to have cooled the North Atlantic relative to warmer conditions during the preceding Bølling-Allerød (14.6-12.9 ka) and after the end of the Younger Dryas when AMOC was stronger (McManus et al., 2004). Northern and Southern Hemisphere averages of globally distributed paleo-temperature records (Fig. 6c) show that the Northern Hemisphere cooled relative to the Southern Hemisphere (Shakun et al., 2012) during Younger Dryas and the many records suggest the Indo-Pacific and global ITCZ shifted south in response. For example, Chinese speleothems, northern Chinese Pollen records (Fig. 6b), and Cariaco Basin down-core percent titanium show decreased precipitation in the Northern Hemisphere during the Younger Dryas Chronozone, while Australian and Brazilian speleothems show increased precipitation in the Southern Hemisphere (Haug et al., 2001; Wang et al., 2004; Wang et al., 2007; Denniston et al., 2013; Chen et al., 2015; Cheng et al., 2016) (Fig. 6d). Equatorial Pacific SSS compilations (Fig 6c) show a similar pattern, demonstrating increased salinity in the Northern Hemisphere relative to the Southern Hemisphere during the Younger Dryas (Gibbons et al., 2014). We hypothesize that this southward shift of the Indo-Pacific ITCZ during the Younger Dryas drove a northward migration of the NEC bifurcation latitude and freshened the Sulu Sea thermocline from ~12.2-11.5 ka. Relatively fresh conditions and the apparent southerly position of the NEC bifurcation latitude during the preceding and following intervals can therefore be attributed to the relatively northerly position of the Ind-Pacific ITCZ.

There is also evidence that a southward migration of the ITZ was responsible for the northward migration of the NEC bifurcation latitude, weakening of the Kuroshio, and increase in Sulu Sea thermocline salinity from ~9.5-8.5 ka. Several century-scale North Atlantic cooling events have been observed in Greenland ice core records at 8.2 ka, 9.3 ka, and 9.95 ka (Rasmussen et al., 2007). Many paleo-precipitation reconstructions have been interpreted to show short term shifts of the ITCZ including in the Indo-Pacific during these cold intervals observed in Greenland ice records. For example, speleothem $\delta^{18}O$ precipitation records from China, Oman, and Brazil show century scale reductions in Northern Hemisphere monsoonal precipitation and an increase in Southern Hemisphere precipitation during the 8.2 ka event (Cheng et al., 2009). Chinese speleothems also show a reduction in precipitation at ~9.2 ka (Cheng et al., 2016) (Fig. 6b). Several other records suggest longer southward shifts of the ITCZ during this interval. Although the authors argue that any Holocene variability isn't statistically significant, equatorial Pacific SSS compilations (Fig. 6c) indicate decreased precipitation in the Northern Hemisphere relative to the Southern Hemisphere from ~10-8 ka (Fig. 6c). Chinese lake core pollen, and a reduction of paleosol formation in the Chinese Loess Plateau indicate a precipitation minimum in the Northern Hemisphere from ~9.5-8.5 ka and ~10-9 ka respectively (Wang et al., 2014; Chen et al., 2015) (Fig. 6c). These paleo-precipitation reconstructions show clear evidence that the Indo-Pacific ITCZ was shifted south for at least part of the ~9.5-8.5 ka interval.

4.2.2 ENSO

ENSO is considered the dominant control on modern interannual NEC bifurcation latitude and as such, millennial scale changes in the mean state of ENSO or the frequency or intensity of El Niño or La Niña events would likely produce changes in the wind field sufficient to shift the NEC bifurcation latitude. However, while there is general consensus on the timing and direction of meridional shifts of the global and Indo-Pacific ITCZ since the LGM, there less consensus on the behavior of ENSO (Koutavas et al., 2002; Rein et al., 2005; Koutavas and Joanides., 2012; Ford et al., 2015; Partin et al., 2015; White et al., 2018). As such, whether ENSO appears to be driving the NEC bifurcation latitude shifts we observe or the two appear to vary asynchronously is dependent on our choice of paleo-ENSO records and it is difficult to identify ENSO as a major driver of NEC bifurcation latitude variability since the LGM.

5. Conclusions

Our analysis of instrumental salinity and sea surface height-based NEC bifurcation latitude records shows that Sulu Sea thermocline salinity is strongly correlated to the NEC bifurcation latitude, increasing when the bifurcation is north and freshening when the bifurcation latitude is south. Our *G. tumida* $\delta^{18}O_{w\text{-}ICV}$ based record of Sulu Sea thermocline salinity shows that NEC bifurcation latitude migrations have occurred on a millennial scale at least since the Last Glacial Maximum. Our Sulu Sea results indicate that the NEC bifurcation latitude was positioned further north around the time of HS1 from ~18.8-15.5 ka, during the Younger Dryas Chronozone from ~12.2-11.5 ka, and during the early Holocene from ~9.5-8.5 ka. The bifurcation latitude was shifted south during the Bølling-Allerød from ~13.0-12.4 ka, during the early Holocene ~11.5-10.9 ka and during the mid-Holocene from ~8.5 ka until the end of the record at ~5.6 ka. Comparison of our paleo-reconstruction of the NEC bifurcation latitude to other paleoclimate records suggests that the observed millennial-scale NEC bifurcation latitude variability may have been driven by the same mechanisms that resulted in the interannual bifurcation latitude variability observed in instrumental records. The most likely driver of the millennial-scale shifts in the NEC bifurcation latitude is the Indo-Pacific ITCZ which was shifted south during HS1, the Younger Dryas, and the 8.2 ka event all when our record suggests the NEC bifurcation latitude was shifted north. The Indo-Pacific ITCZ was shifted north during the Bølling-Allerød and early Holocene when our record indicates the NEC bifurcation latitude was shifted south. There is also some evidence that ENSO contributed to modulating the NEC bifurcation latitude. Such variability of the NEC bifurcation latitude has the potential to substantially affect the strength of the Kuroshio Current, northwest Pacific climate, and the characteristics of the ITF.

Acknowledgments

This work was supported by National Science Foundation [grant number OCE-1736602] to B.K.L. The authors thank Jonathan Vasquez for efforts processing samples and Jerry McManus for assistance with data interpretation. We also thank Wei Huang and Angela Dial for their assistance analyzing samples. Data are in the process of being uploaded to the NOAA World Data Service for Paleoclimatology (https://www.ncdc.noaa.gov/paleo-search/).

References

Adler, R.F., Huffman, G.J., Chang, A., Ferraro, R., Xie, P.-P., Janowiak, J., Rudolf, B., Schneider, U., Curtis, S., Bolvin, D., Gruber, A., Susskind, J., Arkin, P., Nelkin, E., 2003. The Version-2 Global Precipitation Climatology Project (GPCP) Monthly Precipitation Analysis (1979–Present). JOURNAL OF HYDROMETEOROLOGY 4, 21.

Anand, P., Elderfield, H., Conte, M.H., 2003. Calibration of Mg/Ca thermometry in planktonic foraminifera from a sediment trap time series. Paleoceanography 18, 1050. https://doi.org/10.1029/2002PA000846

Barker, S., Greaves, M., Elderfield, H., 2003. A study of cleaning procedures used for foraminiferal Mg/Ca paleothermometry. Geochem. Geophys. Geosyst. 4, 8407. https://doi.org/10.1029/2003GC000559

Beaufort, L., de Garidel-Thoron, T., Linsley, B., Oppo, D., Buchet, N., 2003. Biomass burning and oceanic primary production estimates in the Sulu Sea area over the last 380 kyr and the East Asian monsoon dynamics. Marine Geology 201, 53–65. https://doi.org/10.1016/S0025-3227(03)00208-1

Behringer, D., Xue, Y., 2004. Evaluation of the global ocean data assimilation system at NCEO: The Pacific Ocean 6.

Bemis, B.E., Spero, H.J., Bijma, J., Lea, D.W., 1998. Reevaluation of the oxygen isotopic composition of planktonic foraminifera: Experimental results and revised paleotemperature equations. Paleoceanography 13, 150–160. https://doi.org/10.1029/98PA00070

Chen, F., Xu, Q., Chen, J., Birks, H.J.B., Liu, J., Zhang, S., Jin, L., An, C., Telford, R.J., Cao, X., Wang, Z., Zhang, X., Selvaraj, K., Lu, H., Li, Y., Zheng, Z., Wang, H., Zhou, A., Dong, G., Zhang, J., Huang, X., Bloemendal, J., Rao, Z., 2015. East Asian summer monsoon precipitation variability since the last deglaciation. Sci Rep 5, 11186. https://doi.org/10.1038/srep11186

Chen, H.-F., Chang, Y.-P., Kao, S.-J., Chen, M.-T., Song, S.-R., Kuo, L.-W., Wen, S.-Y., Yang, T.-N., Lee, T.-Q., 2011. Mineralogical and geochemical investigations of sediment-source region changes in the Okinawa Trough during the past 100ka (IMAGES core MD012404). Journal of Asian Earth Sciences 40, 1238–1249. https://doi.org/10.1016/j.jseaes.2010.09.015

Chen, S., Hoffmann, S.S., Lund, D.C., Cobb, K.M., Emile-Geay, J., Adkins, J.F., 2016. A high-resolution speleothem record of western equatorial Pacific rainfall: Implications for Holocene ENSO evolution. Earth and Planetary Science Letters 442, 61–71. https://doi.org/10.1016/j.epsl.2016.02.050

Cheng, H., Edwards, R.L., Sinha, A., Spötl, C., Yi, L., Chen, S., Kelly, M., Kathayat, G., Wang, X., Li, X., Kong, X., Wang, Y., Ning, Y., Zhang, H., 2016. The Asian monsoon over the past 640,000 years and ice age terminations. Nature 534, 640–646. https://doi.org/10.1038/nature18591

Cheng, H., Fleitmann, D., Edwards, R.L., Wang, X., Cruz, F.W., Auler, A.S., Mangini, A., Wang, Y., Kong, X., Burns, S.J., Matter, A., 2009. Timing and structure of the 8.2 kyr B.P. event inferred from δ18O records of stalagmites from China, Oman, and Brazil. Geology 37, 1007–1010. https://doi.org/10.1130/G30126A.1

Cheng, H., Zhang, H., Spötl, C., Baker, J., Sinha, A., Li, H., Bartolomé, M., Moreno, A., Kathayat, G., Zhao, J., Dong, X., Li, Y., Ning, Y., Jia, X., Zong, B., Ait Brahim, Y., Pérez-Mejías, C., Cai, Y., Novello, V.F., Cruz, F.W., Severinghaus, J.P., An, Z., Edwards, R.L., 2020. Timing and structure of the Younger Dryas event and its underlying climate dynamics. Proc Natl Acad Sci USA 117, 23408–23417. https://doi.org/10.1073/pnas.2007869117

Clark, P.U., Mitrovica, J.X., Milne, G.A., Tamisiea, M.E., 2002. Sea-Level Fingerprinting as a Direct Test for the Source of Global Meltwater Pulse IA. Science, New Series 295, 2438–2441.

Clark, P.U., Mix, A.C., 2002. Ice sheets and sea level of the Last Glacial Maximum. Quaternary Science Reviews 7.

Craig, H., Gordon, L., 1965. Deuterium and oxygen 18 variations in the ocean and marine atmosphere.

Dang, H., Jian, Z., Bassinot, F., Qiao, P., Cheng, X., 2012. Decoupled Holocene variability in surface and thermocline water temperatures of the Indo-Pacific Warm Pool. Geophys. Res. Lett. 39, L01701. https://doi.org/10.1029/2011GL050154

Dannenmann, S., Linsley, B.K., Oppo, D.W., Rosenthal, Y., Beaufort, L., 2003. East Asian monsoon forcing of suborbital variability in the Sulu Sea during Marine Isotope Stage 3: Link to Northern Hemisphere climate. Geochem. Geophys. Geosyst. 4, 1–13. https://doi.org/10.1029/2002GC000390

de Garidel-Thoron, T., Beaufort, L., Linsley, B.K., Dannenmann, S., 2001. Millennial-scale dynamics of the east Asian winter monsoon during the last 200,000 years. Paleoceanography 16, 491–502. https://doi.org/10.1029/2000PA000557

Denniston, R.F., Wyrwoll, K.-H., Asmerom, Y., Polyak, V.J., Humphreys, W.F., Cugley, J., Woods, D., LaPointe, Z., Peota, J., Greaves, E., 2013. North Atlantic forcing of millennial-scale Indo-Australian monsoon dynamics during the Last Glacial period. Quaternary Science Reviews 72, 159–168. https://doi.org/10.1016/j.quascirev.2013.04.012

Dou, Y., Yang, S., Liu, Z., Clift, P.D., Yu, H., Berne, S., Shi, X., 2010. Clay mineral evolution in the central Okinawa Trough since 28ka: Implications for sediment provenance and paleoenvironmental change. Palaeogeography, Palaeoclimatology, Palaeoecology 288, 108–117. https://doi.org/10.1016/j.palaeo.2010.01.040

Ford, H.L., Ravelo, A.C., Polissar, P.J., 2015. Reduced El Nino-Southern Oscillation during the Last Glacial Maximum. Science 347, 255–258. https://doi.org/10.1126/science.1258437

Gibbons, F.T., Oppo, D.W., Mohtadi, M., Rosenthal, Y., Cheng, J., Liu, Z., Linsley, B.K., 2014. Deglacial δ18O and hydrologic variability in the tropical Pacific and Indian Oceans. Earth and Planetary Science Letters 387, 240–251. https://doi.org/10.1016/j.epsl.2013.11.032

Gordon, A., Villanoy, C., 2011. The Oceanography of the Philippine Archipelago: Introduction to the Special Issue. Oceanog 24, 13–13. https://doi.org/10.5670/oceanog.2011.13

Gordon, A.L., Huber, B.A., Metzger, E.J., Susanto, R.D., Hurlburt, H.E., Adi, T.R., 2012. South China Sea throughflow impact on the Indonesian throughflow. Geophys. Res. Lett. 39, L11602. https://doi.org/10.1029/2012GL052021

Gordon, A.L., Tessler, Z.D., Villanoy, C., 2011. Dual overflows into the deep Sulu Sea. Geophys. Res. Lett. 38, L18606. https://doi.org/10.1029/2011GL048878

Haug, G.H., 2001. Southward Migration of the Intertropical Convergence Zone Through the Holocene. Science 293, 1304–1308. https://doi.org/10.1126/science.1059725

Holbourn, A., Kuhnt, W., Xu, J., 2011. Indonesian Throughflow variability during the last 140 ka: the Timor Sea outflow. Geological Society, London, Special Publications 355, 283–303. https://doi.org/10.1144/SP355.14

Hollstein, M., Mohtadi, M., Rosenthal, Y., Moffa Sanchez, P., Oppo, D., Martínez Méndez, G., Steinke, S., Hebbeln, D., 2017. Stable Oxygen Isotopes and Mg/Ca in Planktic Foraminifera From Modern Surface Sediments of the Western Pacific Warm Pool: Implications for Thermocline Reconstructions: Modern WPWP Hydrography. Paleoceanography 32, 1174–1194. https://doi.org/10.1002/2017PA003122

Hu, D., Wu, L., Cai, W., Gupta, A.S., Ganachaud, A., Qiu, B., Gordon, A.L., Lin, X., Chen, Z., Hu, S., Wang, G., Wang, Q., Sprintall, J., Qu, T., Kashino, Y., Wang, F., Kessler, W.S., 2015. Pacific western boundary currents and their roles in climate. Nature 522, 299–308. https://doi.org/10.1038/nature14504

Kim, Y.Y., Qu, T., Jensen, T., Miyama, T., Mitsudera, H., Kang, H.-W., Ishida, A., 2004. Seasonal and interannual variations of the North Equatorial Current bifurcation in a high-resolution OGCM. J. Geophys. Res. 109, C03040. https://doi.org/10.1029/2003JC002013

Koutavas, A., Joanides, S., 2012. El Niño-Southern Oscillation extrema in the Holocene and Last Glacial Maximum. Paleoceanography 27, PA4208. https://doi.org/10.1029/2012PA002378

Koutavas, A., Lynch-Stieglitz, J., Jr., T.M.M., Sachs, J.P., 2002. El Niño-like Pattern in Ice Age Tropical Pacific Sea Surface Temperature. Science 297, 226–230.

Kuehl, S.A., Fuglseth, T.J., Thunell, R.C., 1993. Sediment mixing and accumulation rates in the Sulu and South China Seas: Implications for organic carbon preservation in deep-sea environments. Marine Geology 111, 15–35. https://doi.org/10.1016/0025-3227(93)90186-Y

Li, T., Xu, Z., Lim, D., Chang, F., Wan, S., Jung, H., Choi, J., 2015. Sr–Nd isotopic constraints on detrital sediment provenance and paleoenvironmental change in the northern Okinawa

Trough during the late Quaternary. Palaeogeography, Palaeoclimatology, Palaeoecology 430, 74–84. https://doi.org/10.1016/j.palaeo.2015.04.017

Lin, Y.-S., Wei, K.-Y., Lin, I.-T., Yu, P.-S., Chiang, H.-W., Chen, C.-Y., Shen, C.-C., Mii, H.-S., Chen, Y.-G., 2006. The Holocene Pulleniatina Minimum Event revisited: Geochemical and faunal evidence from the Okinawa Trough and upper reaches of the Kuroshio current. Marine Micropaleontology 59, 153–170. https://doi.org/10.1016/j.marmicro.2006.02.003

Linsley, B.K., 1990. The record of deglaciation in the Sulu Sea: Evidence for the Younger Dryas event in the tropical western Pacific. Paleoceanography 5, 10025–11039.

Linsley, B.K., Rosenthal, Y., Oppo, D.W., 2010. Holocene evolution of the Indonesian throughflow and the western Pacific warm pool. Nature Geosci 3, 578–583. https://doi.org/10.1038/ngeo920

McManus, J.F., Francois, R., Gherardi, J.-M., Keigwin, L.D., Brown-Leger, S., 2004. Collapse and rapid resumption of Atlantic meridional circulation linked to deglacial climate changes. Nature 428, 834–837. https://doi.org/10.1038/nature02494

Mohtadi, M., Oppo, D.W., Lückge, A., DePol-Holz, R., Steinke, S., Groeneveld, J., Hemme, N., Hebbeln, D., 2011. Reconstructing the thermal structure of the upper ocean: Insights from planktic foraminifera shell chemistry and alkenones in modern sediments of the tropical eastern Indian Ocean. Paleoceanography 26, PA3219. https://doi.org/10.1029/2011PA002132

Mohtadi, M., Prange, M., Oppo, D.W., De Pol-Holz, R., Merkel, U., Zhang, X., Steinke, S., Lückge, A., 2014. North Atlantic forcing of tropical Indian Ocean climate. Nature 509, 76–80. https://doi.org/10.1038/nature13196

Oppo, D.W., Linsley, B.K., Rosenthal, Y., Dannenmann, S., Beaufort, L., 2003. Orbital and suborbital climate variability in the Sulu Sea, western tropical Pacific. Geochem. Geophys. Geosyst. 4, 1–20. https://doi.org/10.1029/2001GC000260

Partin, J.W., Cobb, K.M., Adkins, J.F., Clark, B., Fernandez, D.P., 2007. Millennial-scale trends in west Pacific warm pool hydrology since the Last Glacial Maximum. Nature 449, 452–455. https://doi.org/10.1038/nature06164

Partin, J.W., Quinn, T.M., Shen, C.-C., Okumura, Y., Cardenas, M.B., Siringan, F.P., Banner, J.L., Lin, K., Hu, H.-M., Taylor, F.W., 2015. Gradual onset and recovery of the Younger Dryas abrupt climate event in the tropics. Nat Commun 6, 8061. https://doi.org/10.1038/ncomms9061

Qiu, B., Chen, S., 2010. Interannual-to-Decadal Variability in the Bifurcation of the North Equatorial Current off the Philippines. Journal of Physical Oceanography 40, 2525–2538. https://doi.org/10.1175/2010JPO4462.1

Qiu, B., Lukas, R., 1996. Seasonal and interannual variability of the North Equatorial Current, the Mindanao Current, and the Kuroshio along the Pacific western boundary. J. Geophys. Res. 101, 12315–12330. https://doi.org/10.1029/95JC03204

Rasmussen, S.O., Vinther, B.M., Clausen, H.B., Andersen, K.K., 2007. Early Holocene climate oscillations recorded in three Greenland ice cores. Quaternary Science Reviews 26, 1907–1914. https://doi.org/10.1016/j.quascirev.2007.06.015

Rayner, N.A., 2003. Global analyses of sea surface temperature, sea ice, and night marine air temperature since the late nineteenth century. J. Geophys. Res. 108, 4407. https://doi.org/10.1029/2002JD002670

Rein, B., Lückge, A., Reinhardt, L., Sirocko, F., Wolf, A., Dullo, W.-C., 2005. El Niño variability off Peru during the last 20,000 years. Paleoceanography 20, PA4003. https://doi.org/10.1029/2004PA001099

Rosenthal, Y., Boyle, E.A., Slowey, N., 1997. Temperature control on the incorporation of magnesium, strontium, fluorine, and cadmium into benthic foraminiferal shells from Little Bahama Bank: Prospects for thermocline paleoceanography. Geochimica et Cosmochimica Acta 61, 3633–3643. https://doi.org/10.1016/S0016-7037(97)00181-6

Rosenthal, Y., Field, M.P., Sherrell, R.M., 1999. Precise Determination of Element/Calcium Ratios in Calcareous Samples Using Sector Field Inductively Coupled Plasma Mass Spectrometry. Anal. Chem. 71, 3248–3253. https://doi.org/10.1021/ac981410x

Rosenthal, Y., Oppo, D.W., Linsley, B.K., 2003. The amplitude and phasing of climate change during the last deglaciation in the Sulu Sea, western equatorial Pacific. Geophys. Res. Lett. 30, 1428. https://doi.org/10.1029/2002GL016612

Ryan, W.B.F., Carbotte, S.M., Coplan, J.O., O'Hara, S., Melkonian, A., Arko, R., Weissel, R.A., Ferrini, V., Goodwillie, A., Nitsche, F., Bonczkowski, J., Zemsky, R., 2009. Global Multi-Resolution Topography synthesis. Geochem. Geophys. Geosyst. 10, Q03014. https://doi.org/10.1029/2008GC002332

Sagawa et al. - 2012 - Shoaling of the western equatorial Pacific thermoc.pdf, n.d.

Sagawa, T., Yokoyama, Y., Ikehara, M., Kuwae, M., 2012. Shoaling of the western equatorial Pacific thermocline during the last glacial maximum inferred from multispecies temperature reconstruction of planktonic foraminifera. Palaeogeography, Palaeoclimatology, Palaeoecology 346–347, 120–129. https://doi.org/10.1016/j.palaeo.2012.06.002

Sathiamurthy, E., Voris, H.K., 2006. Maps of Holocene Sea level transgression and submerged lakes on the Sunda Shelf. Natural History Journal Chulalongkorn University Suppl. 2, 1–44.

Schmidt, M.W., Spero, H.J., Lea, D.W., 2004. Links between salinity variation in the Caribbean and North Atlantic thermohaline circulation. Nature 428, 160–163. https://doi.org/10.1038/nature02346

Shakun, J.D., Clark, P.U., He, F., Marcott, S.A., Mix, A.C., Liu, Z., Otto-Bliesner, B., Schmittner, A., Bard, E., 2012. Global warming preceded by increasing carbon dioxide concentrations during the last deglaciation. Nature 484, 49–54. https://doi.org/10.1038/nature10915

Smith, C., 2018. Niño 3.4 SST Index [WWW Document]. NOAA ESRL Ohysical Sciences Division. URL https://www.esrl.noaa.gov/psd/gcos_wgsp/Timeseries/Nino34/ (accessed 7.31.18).

Stuvier, M., Reimer, P.J., Reimer, R.W., 2020. CALIB 7.1.

Ujiié, Y., Asahi, H., Sagawa, T., Bassinot, F., 2016. Evolution of the North Pacific Subtropical Gyre during the past 190 kyr through the interaction of the Kuroshio Current with the surface and intermediate waters. Paleoceanography 31, 1498–1513. https://doi.org/10.1002/2015PA002914

Wang, H., Chen, J., Zhang, X., Chen, F., 2014. Palaeosol development in the Chinese Loess Plateau as an indicator of the strength of the East Asian summer monsoon: Evidence for a mid-Holocene maximum. Quaternary International 334–335, 155–164. https://doi.org/10.1016/j.quaint.2014.03.013

Wang, X., Auler, A.S., Edwards, R.L., Cheng, H., Cristalli, P.S., Smart, P.L., Richards, D.A., Shen, C.-C., 2004. Wet periods in northeastern Brazil over the past 210 kyr linked to distant climate anomalies. Nature 432, 740–743. https://doi.org/10.1038/nature03067

Wang, X., Auler, A.S., Edwards, R.L., Cheng, H., Ito, E., Wang, Y., Kong, X., Solheid, M., 2007. Millennial-scale precipitation changes in southern Brazil over the past 90,000 years. Geophys. Res. Lett. 34, L23701. https://doi.org/10.1029/2007GL031149

Wang, Y., Xu, T., Li, S., Susanto, R.D., Agustiadi, T., Trenggono, M., Tan, W., Wei, Z., 2019. Seasonal variation of water transport through the Karimata Strait. Acta Oceanol. Sin. 38, 47–57. https://doi.org/10.1007/s13131-018-1224-2

White, S.M., Ravelo, A.C., Polissar, P.J., 2018. Dampened El Niño in the Early and Mid-Holocene Due To Insolation-Forced Warming/Deepening of the Thermocline. Geophys. Res. Lett. 45, 316–326. https://doi.org/10.1002/2017GL075433

Wu, C.-R., 2013. Interannual modulation of the Pacific Decadal Oscillation (PDO) on the low-latitude western North Pacific. Progress in Oceanography 110, 49–58. https://doi.org/10.1016/j.pocean.2012.12.001

Wu, C.-R., Lin, Y.-F., Qiu, B., 2019. Impact of the Atlantic Multidecadal Oscillation on the Pacific North Equatorial Current bifurcation. Sci Rep 9, 2162. https://doi.org/10.1038/s41598-019-38479-w

Xu, J., 2014. Change of Indonesian Throughflow outflow in response to East Asian monsoon and ENSO activities since the Last Glacial. Sci. China Earth Sci. 57, 791–801. https://doi.org/10.1007/s11430-014-4845-0

Xu, J., Holbourn, A., Kuhnt, W., Jian, Z., Kawamura, H., 2008. Changes in the thermocline structure of the Indonesian outflow during Terminations I and II. Earth and Planetary Science Letters 273, 152–162. https://doi.org/10.1016/j.epsl.2008.06.029

Yokoyama, Y., Esat, T.M., Thompson, W.G., Thomas, A.L., Webster, J.M., Miyairi, Y., Sawada, C., Aze, T., Matsuzaki, H., Okuno, J., Fallon, S., Braga, J.-C., Humblet, M., Iryu, Y., Potts, D.C., Fujita, K., Suzuki, A., Kan, H., 2018. Rapid glaciation and a two-step sea level plunge into the Last Glacial Maximum. Nature 559, 603–607. https://doi.org/10.1038/s41586-018-0335-4

Yu, J., Day, J., Greaves, M., Elderfield, H., 2005. Determination of multiple element/calcium ratios in foraminiferal calcite by quadrupole ICP-MS. Geochem. Geophys. Geosyst. 6, Q08P01. https://doi.org/10.1029/2005GC000964

Zeng, L., Wang, D., Xiu, P., Shu, Y., Wang, Q., Chen, J., 2016. Decadal variation and trends in subsurface salinity from 1960 to 2012 in the northern South China Sea: Decadal Subsurface S Changes in the NSCS. Geophys. Res. Lett. 43, 12,181-12,189. https://doi.org/10.1002/2016GL071439